Image moment-based wavefront sensing for in-situ full-field image quality assessment

Lee, Hanshin, Hill, Gary

Hanshin Lee, Gary J. Hill, "Image moment-based wavefront sensing for in-situ full-field image quality assessment," Proc. SPIE 8450, Modern Technologies in Space- and Ground-based Telescopes and Instrumentation II, 845055 (13 September 2012); doi: 10.1117/12.926739

SPIE.

Event: SPIE Astronomical Telescopes + Instrumentation, 2012, Amsterdam, Netherlands

Image Moment based Wavefront Sensing for *In situ* Full-field Image Quality Assessment

Hanshin Lee[1] and Gary J. Hill

McDonald Observatory, University of Texas at Austin, 2515 Speedway Stop 1402, Austin, TX 78712-0259, USA

ABSTRACT

A new concept of using focus-diverse point spread functions (PSF) for modal wavefront sensing (WFS) is explored. This concept is based on relatively straightforward image moment analysis of measured PSFs, which differentiates it from other focal-plane WFS techniques. The presented geometric analysis shows that the image moments are nonlinear functions of wave aberration coefficients but notes that focus diversity essentially decouples the coefficients of interest from others, resulting in a set of linear equations whose solution corresponds to modal coefficient estimates. The presented simulations suggest the potential of this method in in-situ full field image quality assessment and deterministic alignment control of wide field imaging systems.

Keywords: Image moment, Wavefront sensing, Full field image quality

1. INTRODUCTION

An optical wavefront corresponds to the phase of a light wave field that governs the geometric and diffractive image formation process[1]. During the passage of light through a physical system (such as the Earth's atmosphere or imaging systems), the wave field interacts with various physical states of the system and the phase is deformed, as a result, with the information of the physical states imprinted. The ability to measure wavefront, therefore, can allow one to characterize the system and to rectify its error or to improve its performance in either a closed- or open-loop fashion. Sub-nanometer scale 8-meter-class optical surface metrology[2], precision alignment of complex optical systems[3], and near-diffraction-limited telescopes[4] are just a few examples of how the worldwide science and engineering community have benefited from wavefront-sensing (WFS).

Over the past 20 years, several modern WFS techniques have been applied to metrology applications including testing large telescope mirrors[5], diagnosing human eyes[6], and quantifying atmospheric turbulence[7]. These techniques have become not only the essential tools in high precision optical measurements/control applications, but also an integral part of adaptive and active control of imaging systems. WFS technology is pushing the limit even further and allows us to realize even more ambitious adaptive systems, for example the ones that can enable improving image quality in con-focal microscopy[8] or directly imaging Earth-like planets in astronomy[9]. In the following, we briefly summarize the characteristics of some of the typical WFS techniques to give a brief background of the existing WFS methods.

Interferometry is one of the modern WFS techniques. The interference between coherent monochromatic reference and test beams is the key measurement. This interferogram is a manifestation of the optical path difference between two beams and at least three phase-shifted interferograms need be obtained for unambiguous reconstruction of wrapped (i.e. modulo 2π) phase. Subsequent phase unwrapping reveals the underlying optical path difference, normally referred to as the 'optical wavefront'. Among several types, the Twyman-Green arrangement[10] is often used in interferometric WFS instruments where the target beam probes a system under test and then returns back to interfere with the reference beam, and is thus called double-path interferometry. In principle, this WFS method can provide extremely sensitive wavefront measurement, but the high sensitivity also makes it susceptible to undesired external disturbances (e.g. vibration and airflow). Typical accuracy is limited to around a few tens of nanometers (nm) in root-mean-square (rms) although averaging or instantaneous phase shifting[11] enables accuracy better than a few nm in rms. This becomes a commodity especially in high-precision optical surface metrology.

Quite often, it is desired to use objects within a target scene as the light source of WFS, for example as in adaptive optics. Double-path interferometry is less suitable for such cases due to the obvious fact of the source being inside the interferometer. Instead, a common-path arrangement can be used as in two techniques described in the following: One is shearing interferometry (SHI) where a target beam from a point-like source is collimated and then split into two laterally sheared replicas by a shearing element (e.g. grating or shear plate)[12]. There is an overlapping area between the

[1] Hanshin Lee: E-mail: lee@astro.as.utexas.edu

Modern Technologies in Space- and Ground-based Telescopes and Instrumentation II,
edited by Ramón Navarro, Colin R. Cunningham, Eric Prieto, Proc. of SPIE Vol. 8450, 845055
 · doi: 10.1117/12.926739

two copies, where the interference pattern forms. Unlike double-path interferometry, the interferogram is not the wavefront itself, but a manifestation of wavefront slope variation in a chosen shear direction (thus called shearogram). At least two shearograms need to be measured, respectively in two orthogonal shear directions to characterize the wavefront slope, from which the wavefront error is estimated. The accuracy is determined by the amount of lateral shear and the fringe contrast. The other common-path arrangement leads to point-diffraction interferometry (PDI)[13]. A point-like object is focused onto a pinhole that is large enough to let the object beam pass through, but sufficiently small to diffract a portion of the beam into a diverging spherical beam. Both beams are collimated and then form an interference pattern. The size of the pinhole mainly drives fringe contrast and thus wavefront measurement accuracy[14]. The photon efficiency in PDI is generally known to be inefficient[15][16] although adaptive optics test bench using PDI was reported[17] and a recent PDI method showed a high contrast ratio up to 1000:1 for un-aberrated wavefronts using wired pinholes[18]. With either of these common-path techniques, one is free to choose any appropriate WFS targets through the system under test. This has great advantage over double-path interferometry, in particular when real-time adaptive imaging system control is desired. Although accurate and versatile, interferometry generally requires coherent and nearly monochromatic test sources for WFS. This is certainly feasible in practice via, for instance, using laser sources or narrow band-pass filters. However, in certain situations, one has to live with incoherent and fairly broadband objects to maximize photon signal, for example. Estimating wavefront from interferograms involves rather complicated computational procedures, notably two-dimensional (2D) phase unwrapping, for example. This can be less suitable for applications that require rapid wavefront reconstruction from low signal-to-noise measurements. Various versions of SHI have been implemented to make use of incoherent and extended sources via spatial and temporal modulation techniques[15] although complexity in design, performance optimization, and data analysis in such systems increases as a result.

Shack-Hartmann sensing (SHS), that is a variant of the Hartmann test, offers advantages in both terms of accuracy and simplicity of software and hardware[19]. In SHS, the beam from a test object (usually a point-like source) is collimated and passed through a 2D micro-lens array that is at a reimaged pupil plane of the system. Each micro-lens focuses a particular section of the pupil (a sub-aperture). The centroid position of the focused spot is directly related to the average wavefront slope within the sub-aperture. There is a matrix relation between measured slope and wavefront for a given SHS geometry. Solving the relation for the wavefront, therefore, enables rapid wavefront reconstruction. Because the geometric centroid of each sub-aperture spot is the sole measurement, not only measuring slope is straightforward, but also incoherent and moderately broadband sources are usable. Its WFS accuracy can be comparable to that of interferometry and the hardware arrangement can be simple. All these features make SHS a very popular choice for WFS in practice, especially in adaptive optics.

The above WFS techniques utilize the re-imaged pupil of a system, and are called pupil-plane WFS (PP-WFS). Sometimes, however, pupil re-imaging can be less attractive due to many reasons including space constraints, throughput loss, or the need for WFS at multiple fields. In such cases, Focal-Plane WFS (FP-WFS) techniques can be alternative. Unlike the PP-WFS, the FP-WFS can extract wavefront information from focal plane images captured by the imaging system itself. All objects within the images are potential WFS targets, making access to multiple fields natural and on-the-fly target selection possible, whereas a WFS target needs to be known in advance per sensor in the PP-WFS. This can be particularly attractive, in that the wavefront can vary spatially and temporarily in a random or systematic manner. The ability of rapidly sensing the wavefront distribution across the field of view of an imaging system can certainly increase the possibility of widening the corrected field of view and extracting richer information about the target scene, objects, or the imaging system itself. If the PP-WFS were used, either several sensors have to be populated within the field or a single sensor has to be articulated across the field, complicating a WFS system design and sensor-to-sensor calibration. This is where the FP-WFS can be a better alternative.

Two FP-WFS methods, Curvature Sensing (CS) and Phase Retrieval (PR), are typical. Both work on focus-diverse (i.e. through-focused) focal plane images. In theory, CS requires two extra-focal images to be captured (before and after the focus). The intensity difference between the two are used to derive two quantities: the radial wavefront gradient on the data boundary and wavefront curvature variation inside the boundary[20]. According to the theory of intensity transportation, theses are related to the underlying wavefront via the Poisson equation, when the image formation is approximated by geometric optics[21]. CS has an interesting and advantageous characteristic where the curvature measurement has a direct relation with the voltage distribution of a bimorph deformable mirror[15]. This enables fast control of the mirror in adaptive optics. The amount of focus-diversity, i.e. extra-focal distance, is one of the key parameters that determine the accuracy in CS. Although system-specific, a relatively long extra-focal distance (20mm ~ 200mm) is often necessary in practice to make the geometric approximation valid[15]. A long extra-focal distance could limit the accessibility to different fields for the reason that object images are more likely to overlap with each other

although the optimal choice of the extra-focal distance has been extensively investigated[22]. On the other hand, PR uses a starkly different approach where the wavefront is optimized until its synthetic images closely approximate the measured focus-diverse images[23]. It can be not only accurate, but also flexible in terms of the number of parameters that can be estimated simultaneously (e.g. phase, amplitude, object shape, pupil shape and so on). It has a drawback, though, that a large amount of Fast-Fourier transform (FFT) based calculations may need to occur during the optimization. This can be a formidable task and potentially makes PR a less attractive option in rapid WFS applications when compared to other WFS techniques[15], although a linearized version of PR has been shown to be effective in rapid WFS when the wavefront error is small[24]. In practice, the uniqueness of the wavefront solution can be a concern.

These existing WFS techniques are at the heart of existing adaptive and metrology systems. While their use of a single object at a particular field and time has been effective in many circumstances, more attention is now being paid to accomplishing the same metrology over as much field of view of the system as possible[8][26][27]. This wide-field wavefront sensing is essential but, at the same time, a new challenge for future adaptive imaging systems. From the characteristics of the existing WFS techniques, it is clear that further development is necessary to reach this goal and we believe that a WFS technique using focal-plane images can be the most optimal because of the aforementioned favorable characteristics of the FP-WFS. In this line of thinking, we recognize less attractive features of the existing FP-WFS methods, and have recently come up with a different way of utilizing focal plane images and developed the concept and theory of this new technique[28].

2. IMAGE MOMENT WAVEFRONT SENSING (iWFS)

The iWFS is a new type of modal wavefront sensing technique that utilizes focal-plane images. The sensed quantities are wave aberration coefficients. Compared to the other FP-WFS, the iWFS differs in the way of utilizing the focal-plane images. The main measurement of the iWFS is the k^{th} moment of the image of an object. If the image is considered as a 2D distribution of light, the moments simply tell us about the geometric shape of the distribution. For example, the 1st moment (i.e. centroid) corresponds to the systematic image shift, and the 2nd moment (variance) describes the systematic spread of the distribution. As the order k grows, the finer details of the distribution shape are revealed, e.g. skewness and kurtosis. Measuring moments from an image is merely a simple extension of measuring the centroid or full-width-half-maximum (FWHM) of a point spread function (PSF) and thus can permit rapid WFS.

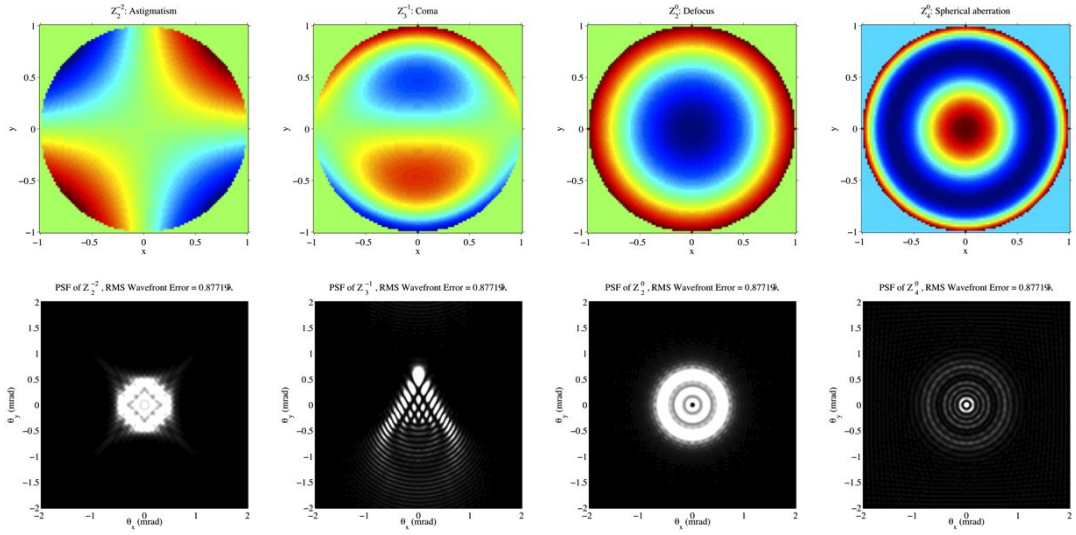

Figure 1 Example wavefront aberrations (top row) and their corresponding point spread functions (bottom row). astigmatism, coma, defocus, and spherical aberration (from left to right).

2.1. Point source case

Geometrically, a system free from aberrations focuses rays from a point object onto a point image. With non-zero wavefront aberrations, rays are spread around and a blurred image results. Each different aberration changes the image shape in a uniquely different way as in Figure 1. This means that there must be some relation between image shapes and wavefront aberrations, which we can understand by looking at how ray aberration arises from wavefront aberration.

Suppose that the wavefront (Φ) from a point source at a particular field on a circular pupil, Ω, is expressed in terms of a weighted linear combination of M Zernike polynomials (Z_i) that are functions of pupil coordinates (h_x, h_y).

$$\Phi = \sum_{i=1}^{M} W_i \, Z_i(h_x, h_y), \tag{1}$$

where W_i is the i-th wave aberration coefficient. The ray coordinates (X, Y) at the focus are given by the first derivative of the wavefront with respect to the pupil coordinates.

$$X = 2F \frac{\partial \Phi}{\partial h_x} = 2F\vec{W}\,\mathbf{D}\,\vec{Z} = \vec{A}^T\,\vec{Z} \quad \text{and} \quad Y = 2F \frac{\partial \Phi}{\partial h_y} = 2F\vec{W}\,\mathbf{E}\,\vec{Z} = \vec{B}^T\,\vec{Z} \tag{2}$$

where F is the focal ratio of the system. This equation essentially defines the geometric image distribution of light for a point object. Here, we used Noll's finding that the derivatives of Z_i can be given in terms of Z_i through the conversion matrices **D** and **E**[29]. When the aberration coefficient vector is multiplied to the conversion matrices, wavefront slope aberration coefficients (vectors A and B) result, whose elements are related to W_i (see Eq. 3 for example).

$$\begin{aligned}
A_1 &= 2W_2 + 2\sqrt{2}W_8 & B_1 &= 2W_3 + 2\sqrt{2}W_7 \\
A_2 &= 2\sqrt{3}W_4 + \sqrt{6}W_6 & B_2 &= \sqrt{5}W_5 + \sqrt{10}W_{13} \\
A_3 &= \sqrt{5}W_5 + \sqrt{10}W_{13} & B_3 &= 2\sqrt{3}W_4 - \sqrt{6}W_6 \\
A_4 &= 2\sqrt{6}W_8 & B_4 &= 2\sqrt{6}W_7 \\
A_5 &= 2\sqrt{3}W_7 + 2\sqrt{3}W_9 & B_5 &= 2\sqrt{3}W_8 - 2\sqrt{3}W_{10} \\
A_6 &= 2\sqrt{3}W_8 + 2\sqrt{3}W_{10} & B_6 &= -2\sqrt{3}W_7 + 2\sqrt{3}W_9
\end{aligned}, \tag{3}$$

One straightforward way of quantifying the shape of the image distribution is to compute the k^{th} image moment as given generally as,

$$\mu_{nm} = \frac{1}{S}\int_{\Omega} I\,(X-\mu_{10})^n\,(Y-\mu_{01})^m\,\mathrm{d}\Omega, \tag{4}$$

Here I is the pupil illumination and the 0th moment S corresponds to the total illumination. μ_{10} and μ_{01} are the 1st image moments. Apparently, μ_{nm} is non-linear in A_i and B_i for $k > 1$. However, there are terms at order k that contain $(A_2)^{\alpha}(B_3)^{\beta}$ multiplied by A_j or B_j such that $k = \alpha + \beta + 1$. As in Eq. 3, A_2 and B_3 are the only coefficients affected by defocus aberration (W_4). Therefore, the k-1th partial derivative of those terms with respect to W_4 decouples A_j or B_j from others. For example, μ_{nm} for k=2 are given as,

$$\mu_{20} = \sum_{i=2}^{M} A_i^2, \;\; \mu_{11} = \sum_{i=2}^{M} A_i\,B_i, \;\; \mu_{02} = \sum_{i=2}^{M} B_i^2, \tag{5}$$

and their first derivatives with respect to W_4 are

$$\frac{\partial \mu_{20}}{\partial W_4} = 4\sqrt{3}A_2, \; \frac{\partial \mu_{11}}{\partial W_4} = 4\sqrt{3}A_3, \; \frac{\partial \mu_{02}}{\partial W_4} = 4\sqrt{3}B_3, \tag{6}$$

We note that $A_3 = B_2$ from Eq. 3. As another example, the second partial derivatives of μ_{nm} for k=3 with respect to W_4 are given as the following:

$$\begin{aligned}
&\frac{\partial^2 \mu_{30}}{\partial W_4^2} = 12\sqrt{3}(A_4 + \sqrt{2}A_6), \; \frac{\partial^2 \mu_{12}}{\partial W_4^2} = 4\sqrt{3}(5A_4 - 3\sqrt{2}A_6), \\
&\frac{\partial^2 \mu_{21}}{\partial W_4^2} = 4\sqrt{3}(5B_4 + 3\sqrt{2}B_6), \; \frac{\partial^2 \mu_{03}}{\partial W_4^2} = 12\sqrt{3}(B_4 - \sqrt{2}B_6), \\
&\text{with} \;\; A_5 = \sqrt{2}B_4 + B_6 \;\; \text{and} \;\; B_5 = \sqrt{2}A_4 + A_6,
\end{aligned} \tag{7}$$

Solving the above results in the slope aberration coefficients that can be used to solve for wavefront coefficients via the relations between the wave and slope coefficients in Eq. 2. Likewise, the k-1th partial derivatives of the k^{th} moments with respect to the wavefront defocus can be used to determine the slope aberrations and subsequently wavefront

aberrations up to order k. From a practical point of view, the moment measurement is just an extension of the image centroid calculation. Thus the computation can be simple and straightforward.

The partial derivative with respect to W4 means focus-diversity. Through-focusing a focal plane is one practical way to achieve focus-diversity. In this simplest implementation, one needs to record the image of an object at k different extra-focal planes and the amount of focus diversity is $\Delta W_4 = \Delta L/(16\sqrt{3}F^2)$ where ΔL is the amount of focal plane shift. This then allows one to express the k^{th} moment as a function of ΔW_4. It can be fit by the k^{th} order polynomial to determine the partial derivatives up to order k-1, which are essentially the fitting coefficients. Another way of achieving focus-diversity is to use an active optical element, such as deformable mirrors or liquid crystal lenses, which is needed anyway for adaptive image compensation, for example. The focal plane can be fixed in position in such cases. The following table summarizes the number of focus-diversities for aberrations up to order k.

Table 1 The number of focus-diversities (N) for determining aberration coefficients up to order k.

k	N	Moments	Slope coefficients	Wave coefficients
1	1	$\mu_{1,0}\ \mu_{0,1}$	$A_1\ B_1$	$W_2\ \ W_3$
2	2	$\mu_{2,0}\ \mu_{1,1}\ \mu_{0,2}$	$A_2\ A_3\ B_2\ B_3$	$W_4\ \ W_5\ \ W_6$
3	3	$\mu_{3,0}\ \mu_{2,1}\ \mu_{1,2}\ \mu_{0,3}$	$A_4\ A_5\ A_6\ B_4\ B_5\ B_6$	$W_7\ \ W_8\ \ W_9\ \ W_{10}$
4	4	$\mu_{4,0}\ \mu_{3,1}\ \mu_{2,2}\ \mu_{1,3}\ \mu_{0,4}$	$A_7\ A_8\ A_9\ A_{10}\ \ B_7\ B_8\ B_9\ B_{10}$	$W_{11}\ W_{12}\ W_{13}\ W_{14}\ W_{15}$
5	5	$\mu_{5,0}\ \mu_{4,1}\ \mu_{3,2}\ \mu_{2,3}\ \mu_{1,4}\ \mu_{0,5}$	$A_{11}\ A_{12}\ A_{13}\ A_{14}\ A_{15}\ \ B_{11}\ B_{12}\ B_{13}\ B_{14}\ B_{15}$	$W_{16}\ W_{17}\ W_{18}\ W_{19}\ W_{20}\ W_{21}$
6	6	$\mu_{6,0}\ \mu_{5,1}\ \mu_{4,2}\ \mu_{3,3}\ \mu_{2,4}\ \mu_{1,5}\ \mu_{0,6}$	$A_{16}\ A_{17}\ A_{18}\ A_{19}\ A_{20}\ \ B_{16}\ B_{17}\ B_{18}\ B_{19}\ B_{20}$	$W_{22}\ W_{23}\ W_{24}\ W_{25}\ W_{26}\ W_{27}\ W_{28}$
7	7	$\mu_{7,0}\ \mu_{6,1}\ \mu_{5,2}\ \mu_{4,3}\ \mu_{3,4}\ \mu_{2,5}\ \mu_{1,6}\ \mu_{0,7}$	$A_{21}\ A_{22}\ A_{23}\ A_{24}\ A_{25}\ A_{26}\ \ B_{21}\ B_{22}\ B_{23}\ B_{24}\ B_{25}\ B_{26}$	$W_{29}\ W_{30}\ W_{31}\ W_{32}\ W_{33}\ W_{34}\ W_{35}\ W_{36}$

2.2. Extended and multiple source case

For the iWFS to be useful, it should be able to utilize not only a point source object, but also an extended source or multiple objects across the field. In this case, Eq. 1 is re-written as the following.

$$\Phi = \sum_{i=1}^{M} \left(w_i + \omega_i\right) Z_i(h_x, h_y), \tag{8}$$

where W_i in Eq. 1 now consists of a field dependent (w_i) and field constant (ω_i) term. This results in the field dependent (a, b) and constant (α, β) slope coefficient vectors.

$$X = 2F\sum_{i=1}^{M}\left\{\sum_{j=1}^{i}(w_i+\omega_i)D_{ij}Z_j\right\} = \left(\vec{a}+\vec{\alpha}\right)^T\vec{Z} \quad \text{and} \quad Y = 2F\sum_{i=1}^{M}\left\{\sum_{j=1}^{i}(w_i+\omega_i)E_{ij}Z_j\right\} = \left(\vec{b}+\vec{\beta}\right)^T\vec{Z}, \tag{9}$$

For an object that occupies a finite region (Λ) on the field of view, the k^{th} image moment is expressed as,

$$\nu_{nm} = \left\{\int\!\!\int_{\Lambda\,\Omega} J\left(X-\nu_{10}\right)^n\left(Y-\nu_{01}\right)^m \mathrm{d}\Omega\,\mathrm{d}\Lambda\right\} \Big/ \left\{\int\!\!\int_{\Lambda\,\Omega} J\,\mathrm{d}\Omega\,\mathrm{d}\Lambda\right\}, \tag{10}$$

J is the true illumination of the object over both Λ and Ω, thus depends on field and pupil coordinates. The denominator corresponds to the total field illumination of the object. Generally, ν_{nm} can be given as the sum of the field constant and dependent part, where the former equals μ_{nm} as in Eq. 4.

$$\nu_{nm} = \mu_{nm} + \tau_{nm} \tag{11}$$

The field dependent moment term, τ_{nm}, can be known only if J over Λ is known. This is nearly impossible in reality without prior wavefront correction or knowledge about the object although, in certain optical metrology cases, the object can be a well calibrated target like a USAF plate. Fortunately, it is often the case that the object region Λ is sufficiently small as compared to the size of the field that wavefront aberration over Λ is either nearly constant or spatially changes very slowly, i.e. $\nu_{nm} \approx \mu_{nm} \gg \tau_{nm}$. Then, it is possible to determine the aberration coefficients as above for the point source case. When the wavefront aberration does change rapidly over the field of interest, if there exist neighboring objects that meet the aforesaid condition, it should be possible to determine the distribution of wavefront aberrations across the field of interest by applying the same moment analysis to these surrounding objects and then to correct for it. In the following section, we present a few example case studies.

3. CASE STUDIES

3.1. Point Source Case

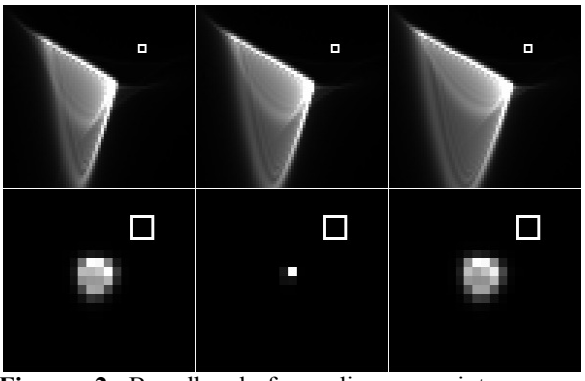

Figure 2 Broadband focus-diverse point source images at three focal planes. (Top) initial; (Bottom) after correction; (Left) 1mm before focus; (Middle) at focus; (Right) 1mm after focus.

In this case, the first nine wavefront aberration coefficients (W_i with i=2,3,4…10) are estimated by using three focus-diverse images sampled in focal planes at -1mm, 0mm, and +1mm away from the nominal focus. The system is assumed to be f/10 with 2.7m aperture diameter. The plate scale is 7.64 arc seconds (″) per mm. The maximum focus-diversity amounts to $\Delta W_f \sim \pm 0.7\lambda$ at λ=514nm. A standard FFT method[30] was used for synthesizing the polychromatic images with uniform spectral weight at 11 wavelengths between 464nm and 564nm. Spectral separation is 10nm between two wavelengths. The moments were computed within a square window with the side length of 5 times the FWHM.

In the top row of Figure 2, the initial point source images at the focal planes are shown. The initial wavefront error amounts to 5.7λ rms. This substantial error makes the focus-diversity effect barely noticeable. The pixel size is 20μm and the white boxes, shown for scale comparison, are 50μm on each side. According to Table 1, one should be able to determine up to W_{10} by using three focus-diverse images. Table 2 summarizes the true and determined aberration coefficients. Note that the slope coefficients (A_i and B_i) are in units of pixel while the wave coefficients are in units of λ. The maximum difference between the true and reduced coefficients is 0.038λ in Z_9. The reduced aberrations were subtracted from the true coefficients (i.e. perfect correction) and the residuals were fed to the FFT image synthesis, resulting in the image in the bottom row of Figure 2. The correction brings a substantial improvement in the point source image.

Table 2 Slope and wave aberration coefficients in Figure 2. Subscript 'red' indicates reduced values and 'tru' means true values

k	Z_i	$A_{i,red}$ [pix]	$A_{i,tru}$ [pix]	$B_{i,red}$ [pix]	$B_{i,tru}$ [pix]	$W_{i,red}$ [λ]	$W_{i,tru}$ [λ]
0	1	-11.924	-11.959	-1.080	-1.144	--	--
1	2	-27.851	-27.986	7.918	7.968	-1.182	-1.185
	3	7.928	7.968	-30.884	-31.015	1.607	1.636
2	4	-12.468	-12.505	-13.006	-13.316	-4.239	-4.241
	5	1.761	1.766	-18.385	-18.601	1.618	1.626
	6	0.753	0.917	20.155	20.598	0.310	0.309
3	7	--	--	--	--	-1.328	-1.359
	8	--	--	--	--	-1.273	-1.276
	9	--	--	--	--	1.582	1.614
	10	--	--	--	--	1.381	1.408

3.2. Extended Source Case

In this case, an extended source (an artificial satellite) image was affected by field constant wavefront error of 3.2λ in rms (Figure 3). The aberrated point-spread-functions (PSF) were synthesized at five planes by the FFT method[30]. The image was then convolved with these PSFs to create aberrated focus-diverse extended source images. The imaging system was assumed f/4 with 0.4m aperture diameter. Photon and read noise of $7e^-$ were added. The pixel size is 4μm. Aberrations up to W_{11} were applied to the synthetic PSFs with equally weighted five wavelengths between 500nm to 600nm. The maximum amount of focus-diversity was about 8.6λ at λ=550nm.

To determine aberration coefficients up to W_{11}, at least four focus-diverse images are necessary. We created five images including the one at the nominal focus, but only used four (top 2 rows and bottom 2 rows in Figure 3). In, the true and reduced wavefront aberration coefficients are compared. Note that the reduced tip/tilt components are in fact a combination of the true wavefront tip/tilt and the centroid of the image. Thus, they were omitted in the subsequent

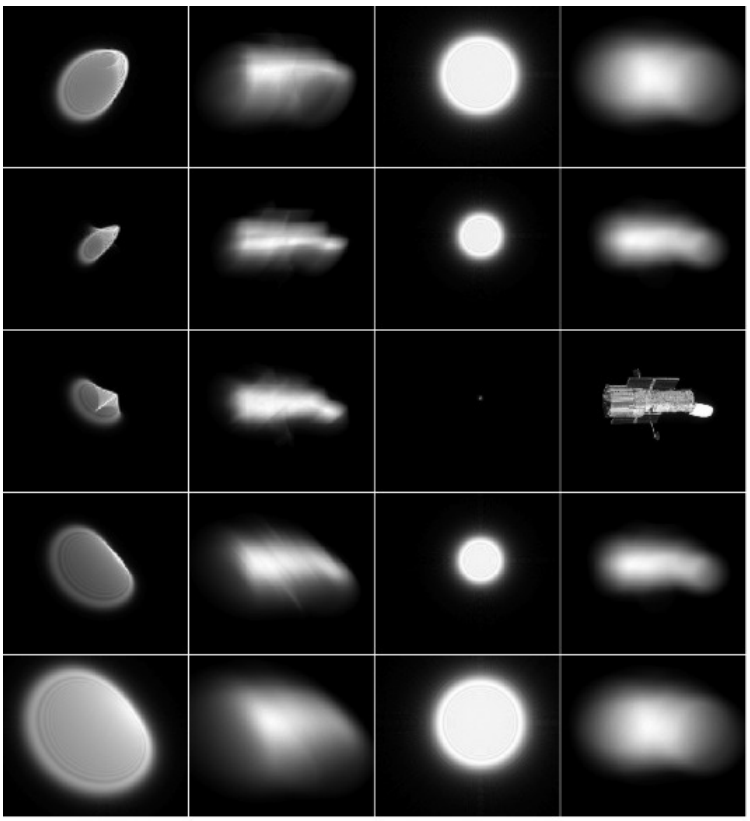

Figure 3 Focus-diverse extended source images. (Far left) Initial aberrated PSFs; (Left) aberrated satellite images; (Right) corrected PSFs; (Far right) corrected images. (Top to bottom) images and PSFs at five different focus-diversities. PSF images are magnified x4.

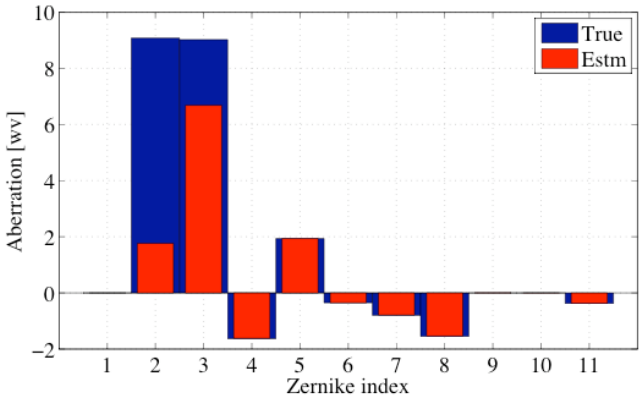

Figure 4 Comparison between the true (blue) and reduced (red) wavefront aberration coefficients for images in Figure 3.

correction. Assuming a perfect wavefront correction, the recovered image is shown in the far right column of Figure 3. In comparison to the initial image in the second left column, great details of the input satellite image are revealed.

3.3. Multiple-Source Case

In some applications, one desires to perform WFS over a wide field of view. For instance, multi-conjugate adaptive optics (MCAO) attempts to measure several WFS stars across a few arc-minute field of view to reconstruct and correct for the 3D atmospheric aberration distribution, thereby widening the corrected field of view[26][31]. In optical alignment and active control, one often needs to verify the off-axis imaging performance of an imaging system, in an open- or closed-loop fashion, because misalignment can introduce field-dependent aberrations that can not be noticed by the usual single field wavefront test only[27]. Enhancing and keeping the image quality across the field is also of paramount importance in con-focal microscopy[32][33]. In all these applications, the ability to sense wavefront across the field of interest is very much important. The iWFS approach can be suitable for such applications due to the fact that it directly deals with as-measured images of the target field as demonstrated below.

On the right panel of Figure 5, we show one of five focus-diverse frames of a simulated star field. The focus-diverse PSFs are shown on the left panel. The star field is 2.6×2.6 square arc minutes (′) in size and assumed to be imaged through a f/9 system with 2.7m aperture diameter. There are total 40 star-like objects in the field, simulating a star field. The stellar magnitude (m_V) varies between 9 and 19.2. The pixel size is 16μm, giving a plate scale of 0.15″ per pixel. Photon noise was added to each frame and the sky background was set to 22 mag. per square arc seconds. For the purpose of demonstrating wide field WFS, field constant wave aberrations up to W_{12} were applied to the image (rms wavefront error of 0.5λ at λ=500nm) and a total five focus-diverse frames were synthesized, with 11 uniformly weighted wavelengths between 500nm and 600nm. The moments were computed within a square analysis window with the side length of 5 times the average FWHM of ~ 6.5 in pixel.

A standard star finding algorithm[34] was used to locate objects in one of the frames. As the focus-diversity does not significantly shift the image from one frame to the others, the locations found there served as the initial centroid of each object in the other frames. We selected analysis stars based on the following. Analysis stars need be distant from

neighboring stars by more than the size of the analysis window. This also served as the minimum distance of a star centroid from the frame edges. The signal-to-noise ratio (SNR) measured within the FWHM of each star needs be higher than 10. Then the moment analysis was carried out for the final candidate stars. Star 004, 005, and 014 are bright enough, but too close to each other or to a frame edge. This can be done every time the field of interest is changed, thereby enabling on-the-fly target acquisition without the prior knowledge of the scene. The moment analysis for the chosen stars was completed in less than five milliseconds.

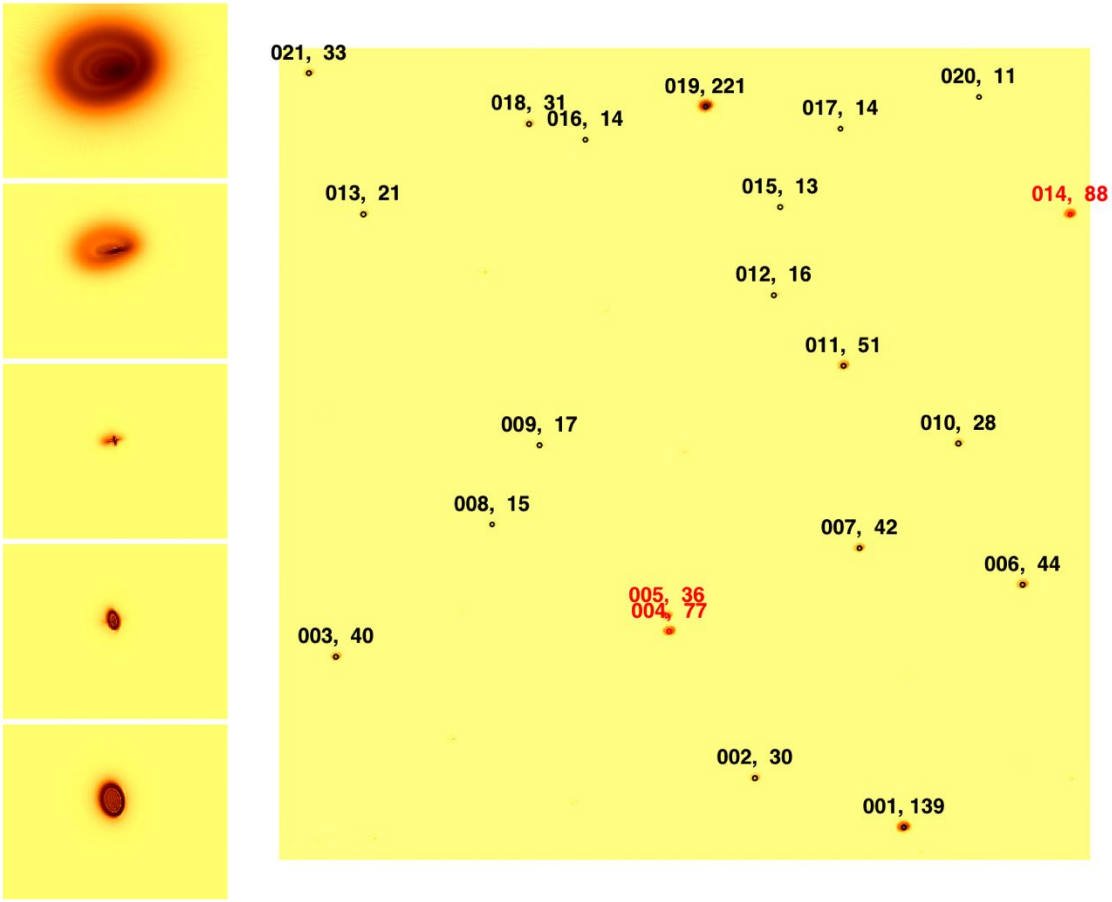

Figure 5 (Left) Five focus-diverse PSFs in a log scale with maximum ΔW_4 of ±1.0λ at top and bottom (λ=550nm). (Right) one of the five focus-diverse frames of a simulated star field in a log scale. A total 40 stars were inserted into a 2.6×2.6 square ′ and m_V ranges from 19.2 to 9. The assumed exposure time is 5 milliseconds per frame. Total 21 stars are labeled with index and SNR value. Star 004 and 005 are too close to each other and 014 is too close to the frame edge. SNR of the analysis stars ranges from 11 to 221 (15.5 to 9 in m_V).

Since there are several objects with different brightness, but the same aberrations, we can determine WFS accuracy as a function of SNR (Figure 6). The blue-solid curve shows the rms value of the difference between the true and reduced aberration coefficients. As we used the standard Zernike coefficients, the rms value corresponds to the rms residual wavefront error. The red dashed curve is a fit of the function $y \sim SNR^{-1}$, which follows the prediction of our current error model as given by the followings

$$E[\mu_i] = \bar{\mu}_i\left(1 + \frac{1}{SNR^2}\right) \quad and \quad Var[\mu_i] = \bar{\mu}_i^2 \frac{2}{SNR^2},$$

where the moment error is inversely proportional to the image signal to noise ratio.

The green dash-dotted curve follows $y \sim SNR^{-0.8}$ whose fitting residual is slightly smaller. These curves simply tell us the universal characteristic of WFS techniques, i.e. higher SNR leads to better accuracy. We have conducted detailed analytical studies to derive the error propagation mechanisms for SNR, target sampling rate (i.e. pixel size), and analysis window size. Some combinations of these could wipe out aberration modes higher than a certain order and thus limit the

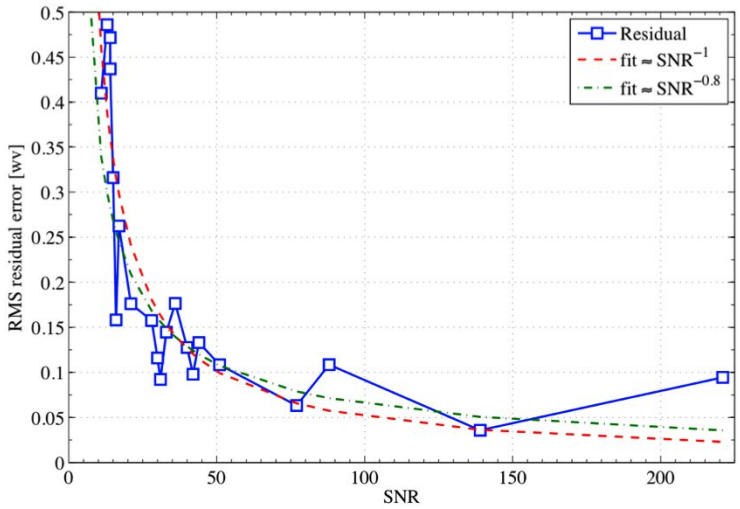

Figure 6 The rms value of the difference between the true and reduced coefficients as a function of SNR of the 21 stars in Figure 5. Two power-law fits ($y \sim SNR^{-1}$ in dashed-red and $y \sim SNR^{-0.8}$ in dash-dotted-green) are overlaid. Note that the SNR value is calculated at zero focus diversity. wv=550nm.

number of useful modes. Deducing more aberrations than can be determined accurately could result in incorrect aberration coefficients. The error propagation analysis will be presented in a separate report.

3.4. Point source through Kolmogorov turbulence

In thic case, we subject a point source to a phase screen with phase fluctuation according to Kolmogorov atmospheric turbulence model. The chosen coherence parameter is r_0=100mm and the telescope is 2.7m in diameter with f/8 beam (0.105mm per arc-second). Here we intend to estimate the first 15 aberration modes. Therefore, 5 focus modulations are needed. Figure 7 show the point source images at 5 different focus modulations (top row). The point source brightness is m_v=11 and 5msec exposure per frame was used. The maximum focus modulation is 1mm. The simulated images are all in Johnson V band. Photon noise and read noise of 2e- were used. The pixel is 0.6 arc-seconds on the sky. In the bottom row, the original phase is shown on the left panel. In the middle, there is a phase screen by 15-term estimate. A gross wavefront error is tip/tilt as expected. After subtracting the estimate from the original phase screen, we obtain a residual phase screen as shown in the right panel. The residual error is 0.2wv is 0.2wv at 500nm and mostly due to un-sensed higher order terms, however the low order terms do show residuals due to un-sensed higher order terms aliasing into the low order modal estimates, which highlights the importance of understanding the higher-order aliasing effect in the presented modal sensing approach.

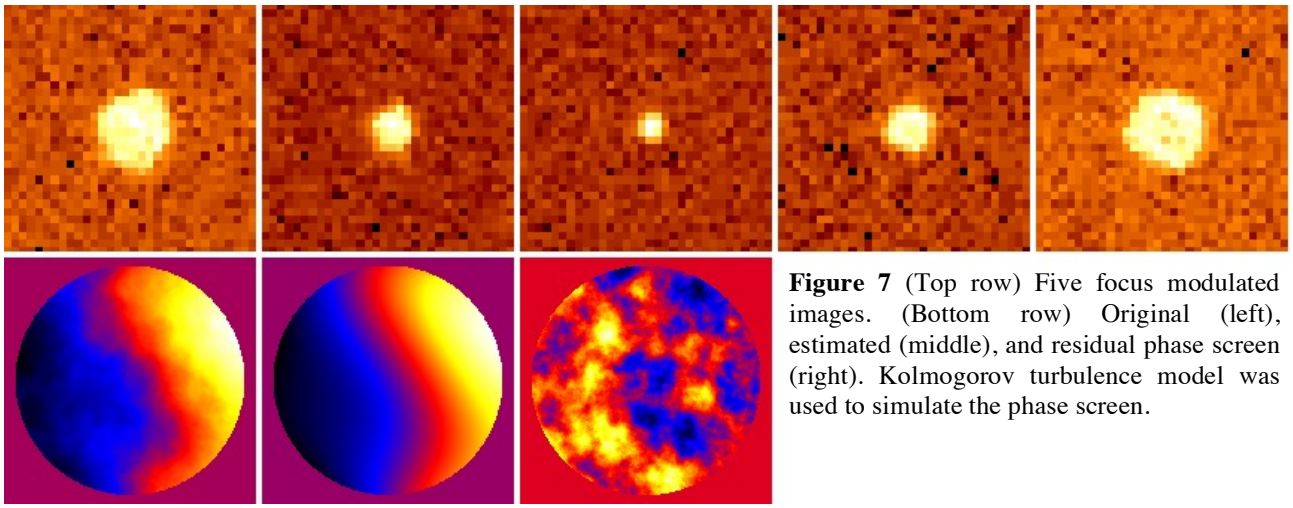

Figure 7 (Top row) Five focus modulated images. (Bottom row) Original (left), estimated (middle), and residual phase screen (right). Kolmogorov turbulence model was used to simulate the phase screen.

4. APPLICATION TO IN SITU IMAGE QUALITY ASSESSMENT

We applied the presented modal sensing technique to a real spectroscopic imaging system called the Visible Integral-field-unit Replicable Unit Spectrograph (VIRUS) instrument. The VIRUS instrument is made up of 150+ individually compact and identical spectrographs, each fed by a fiber integration field unit. The instrument provides integral field spectroscopy from 350nm to 550nm of over 33,600 spatial elements per observation, each 1.8 sq. arcseconds on the sky,

at a spectral resolution of R ~ 700. The instrument will be fed by a new wide-field corrector (WFC) of the Hobby-Eberly Telescope (HET) with increased science field of view as large as 22arcmin diameter and telescope aperture of 10m. The construction of the large number of VIRUS units requires the individual spectrographs be interchangeable at sub-system level and a production line assembly process be utilized, while meeting the optical performance specification.

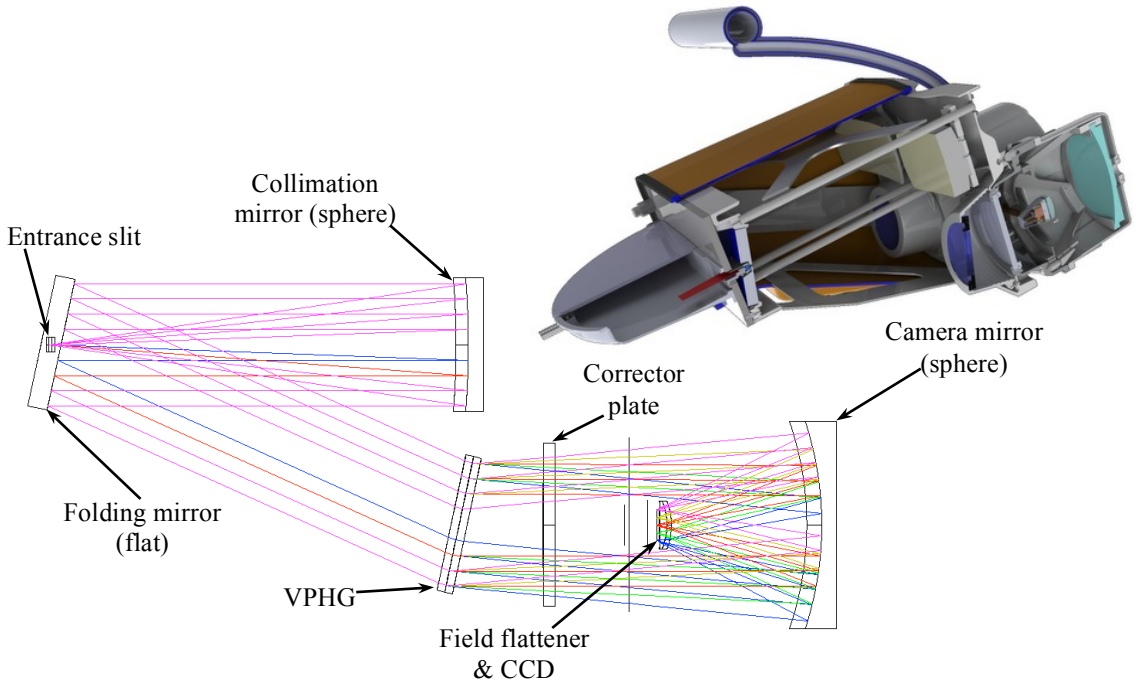

Figure 8 The optical ray trace and rendering of the VIRUS unit spectrograph.

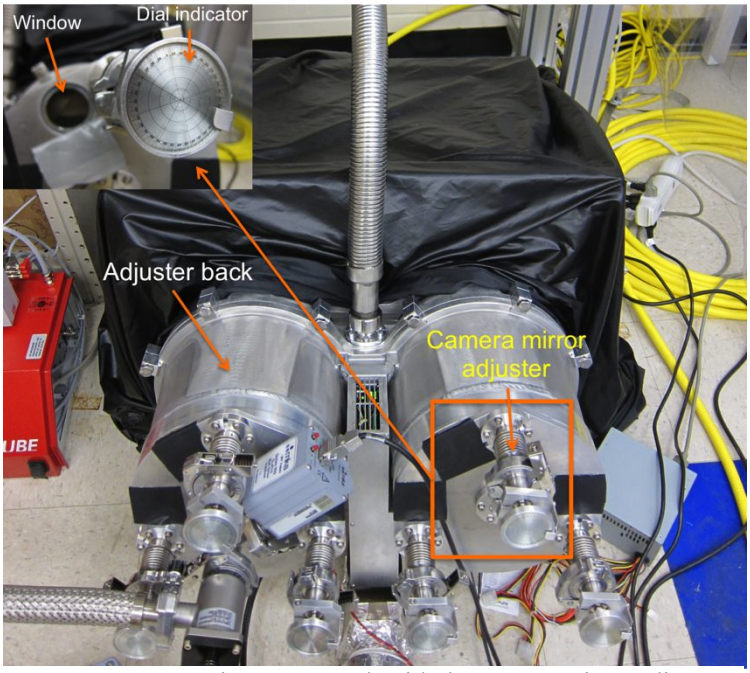

Figure 9 VIRUS unit spectrograph with the camera mirror adjuster back attached for fine alignment.

Figure 8 illustrates the optical layout of the VIRUS unit spectrograph and a sectioned view of the two-unit VIRUS module opto-mechanical model. The optical design of the unit spectrograph is comprised of two sub-systems, both based upon the Schmidt design concept utilizing a Volume Phase Holographic Grating (VPHG). In-depth discussion about the design, tolerance, and construction of the instrument can be found in Ref. [35], [36], and [37].

The system contains two alignment compensators. One is in the collimator. The back of the collimator mirror is glued to a disk plate that is then mounted to a n Aluminum triangular plate. Each corner of this plate has a through hole within which a spherical bearing is attached. The plate then rides on three invar rods through these bearings. Three springs are mounted on the invar rods pushing the plate from the front while three fine-threaded (pitch size of 0.75mm) adjuster screws pushes the plate from the back, separated from each other by 120degrees. Tip, tilt, and focus motions can

be adjusted using these screws. The main purpose of the collimator adjustment is to provide the way to center the collimated beam on the VPHG.

The other adjustment is in the camera mirror. The mirror is held from the side by three knuckle mounts. The front face of the edge of the mirror is pushed from front by a spring plunger inside each knuckle. From behind, we have three fine-threaded (0.7mm pitch size) adjuster screws with hexagonal heads pushing the mirror down. Since the camera system is inside the cryostat, we have a special cryostat cover that has three feed-through with hex-keys attached so that one can adjust the camera mirror screws from outside when the camera system is in vacuum and cold. Each hex-key has a rotation knob with a dial indicator glued. The indicator has 1-degree division mark and a knife-edge plate. This allows us to rotate the knob to place a desired division mark to the knife-edge, thus permitting a resolution of 1/360 turn (i.e. ±2μm in focus motion and ±3arc-seconds in tip/tilt motion). More elaborated discussion about these adjustments can be found in Ref. [38]. Our experience with these adjusters so far indicates that the repeatability is close to 1/120 turn in peak-to-valley. This corresponds to ±6μm in focus and ±9arc-seconds in tip/tilt motion, but is better than the focus requirement of ±10μm and within the tip/tilt requirement of ±10arc-seconds.

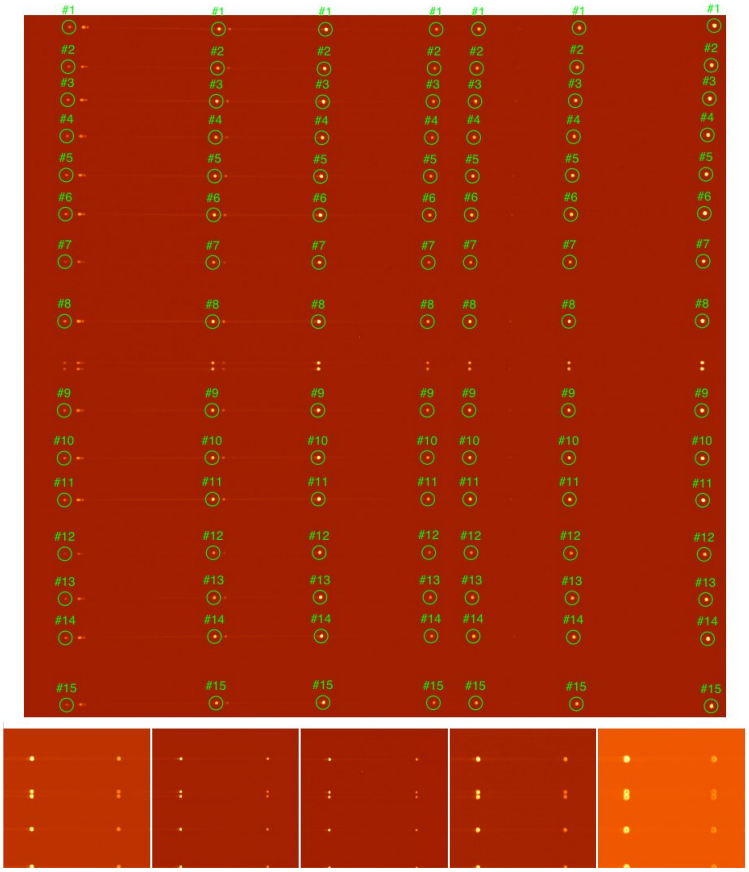

Figure 10 A sample modulation image from the VIRUS unit. (Top) The zero modulation image with fiber target indexes and analysis apertures overlaid. (Bottom) The zoomed-in central sections of 5 modulation images (From left to right, ½ CCW, ¼ CCW, 0, ¼ CW, ½ CW turns of three camera adjusters).

Using the camera mirror adjustment, we are able to modulate the focus aberration to the accuracy of ±0.15 wave (at 632.8nm) in peak-to-valley. Our experience indicates that a half turn (0.35mm in the camera focus) is the appropriate amount of maximum modulation and 5 modulations (at 0, ±1/4, ±1/2 turns) are sufficient to determine the first 15 aberration modes of the spectrograph system since the optical components are expected to have negligible aberration modes higher than order 15 based on the interferometry / profilometry measurements of individual surfaces. The higher-order terms of the design itself are removed through our anti-aliasing process[38]. An example modulation image is shown in Figure 10, showing the fiber core images at discrete emission lines (i.e. the IFU is illuminated by Mercury (Hg) and Cadmium (Cd) emission line lamps) across the CCD (2064×2064 with 15μm pitch). Note that the vertical axis corresponds to the fiber-slit direction and the horizontal axis corresponds to the dispersion direction with the blue end (350nm being near the left edge of the image). In order to aid the modulation, we made an IFU mask that has circular openings for 17 chosen fibers so that each fiber image has enough empty pixels from adjacent fibers in the spatial direction.

The modulated images are passed through a basic reduction pipeline to remove the back ground images, to write appropriate fits header information, and then to adjust the image format since the CCD generates two frames with over-scan areas around them so it is necessary to remove these over-scan areas to properly register one frame to the other. The moment analysis program analyzes the reduced images and produces the first 15 aberration modes. Since the individual optical components are made to the specification, the main interest is to sense any gradient in the low order aberration modes due to misalignment. One example is shown in Figure 11. The top-left plot shows the determined focus aberration across the fiber slit at 7 different wavelengths. It shows a strong focus gradient in the system, amounting 10 wave in peak-to-valley from one end of the slit to the other. The curves are systematically offset by 1 wave. The slope of the curves tells the amount and the direction of the tilt correct

needed for the camera mirror. Once the correction is applied, the curves become flat as shown in the top-right plot. There is a small amount of gradient in the direction of the wavelength, which is negligible thus not corrected. The image quality of the system also reflects this as shown in the bottom plots. Due to the linear focus gradient, the image quality (i.e. full-width at half-maximum of a point spread function) shows a quadratic variation across the fiber slit (Bottom-left). After the tilt correction, the image quality becomes flat as shown in the bottom-right plot.

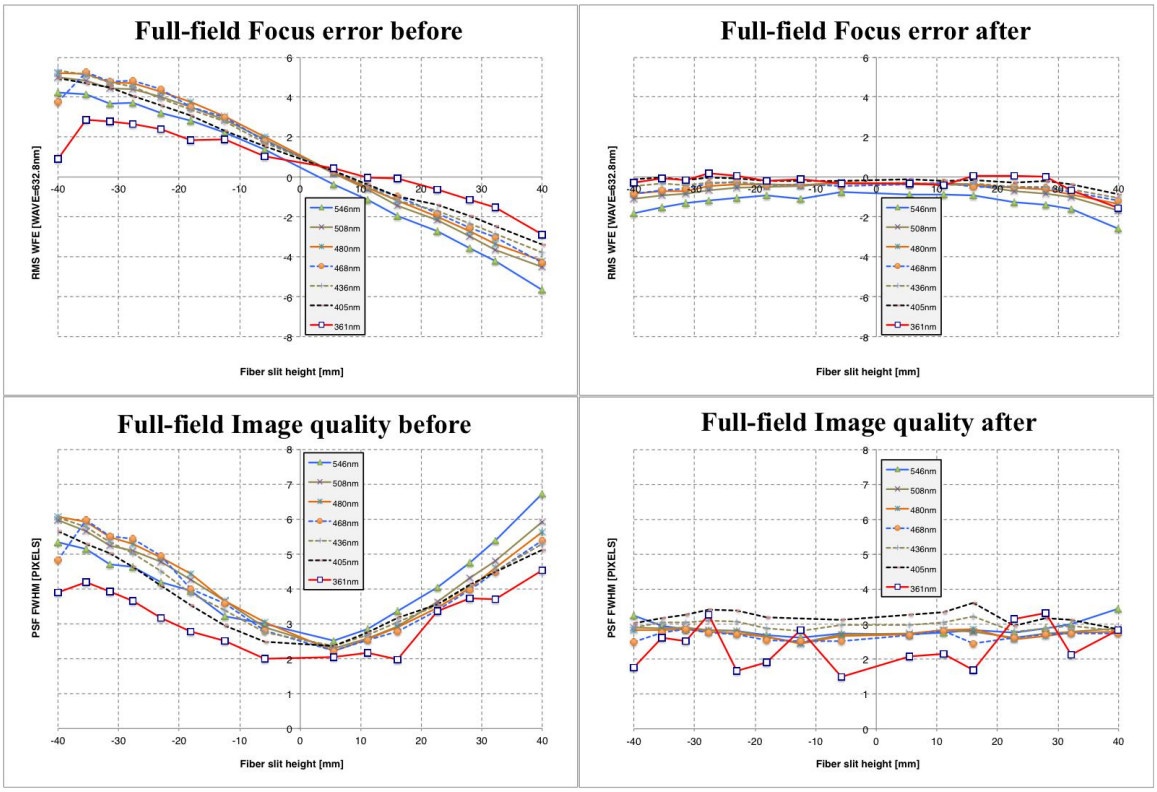

Figure 11 Example analysis results from the moment-based modal sensing of the VIRUS unit spectrograph. Each curve is plotted across the fiber slit at a particular wavelength.

5. SUMMARY

A new concept of using focus-diverse point spread functions (PSF) for modal wavefront sensing (WFS) is presented. This is based on relatively straightforward image moment analysis of measured PSFs, which differentiates it from other focal-plane WFS (FP-WFS) techniques. The presented geometric analysis shows that the image moments are nonlinear functions of wave aberration coefficients but notes that focus diversity essentially decouples the coefficients of interest from others, resulting in a set of linear equations whose solution corresponds to modal coefficient estimates. The presented simulations and application example in a real spectroscopic system suggest the potential of this method for in-situ full field image quality assessment and deterministic alignment control of wide field imaging systems.

ACKNOWLEDGEMENTS

HETDEX is run by the University of Texas at Austin McDonald Observatory and Department of Astronomy with participation from the Ludwig-Maximilians-Universität München, Max-Planck-Institut für Extraterrestriche-Physik (MPE), Leibniz-Institut für Astrophysik Potsdam (AIP), Texas A&M University, Pennsylvania State University, Institut für Astrophysik Göttingen, University of Oxford and Max-Planck-Institut für Astrophysik (MPA). In addition to Institutional support, HETDEX is funded by the National Science Foundation (grant AST-0926815), the State of Texas, the US Air Force (AFRL FA9451-04-2-0355), and generous support from private individuals and foundations.

REFERENCES

[1] Max Born and Emil Wolf, *Principles of Optics* 7th edition (Cambridge, 1999).

[2] S. West, J. Burge, R. Young, D. Anderson, C. Murgiuc, D. Ketelsen, and H. Martin, "Optical metrology for two large highly aspheric telescope mirrors," Appl. Opt. **31**, 7191-7197 (1992).

[3] Hanshin Lee, Gavin B. Dalton, Ian A. J. Tosh, and Sug-Whan Kim, "Computer-guided alignment II :Optical system alignment using differential wavefront sampling," Opt. Express **15**, 15424-15437 (2007).

[4] Marcos A. van Dam, David Le Mignant, and Bruce A. Macintosh, "Performance of the Keck Observatory adaptive-optics system, " Appl. Opt. **43**, 5458-5467 (2004).

[5] Conrad Wells, Gene Olczak, Cormic Merle, Tom Dey, Mark Waldman, Tony Whitman, Eric Wick, and Aaron Peer, "The center of curvature optical assembly for the JWST primary mirror cryogenic optical test," Proc. SPIE 7739, 77390L (2010).

[6] J. Straub, J. Schwiegerling, and A. Gupta, "Design of a compact Shack-Hartmann aberrometer for real-time measurement of aberrations in human eyes," in Vision Science and its Applications, A. Sawchuk, ed., Vol. **53** of OSA Trends in Optics and Photonics (Optical Society of America, 2001), paper SuD3.

[7] M. Schöck, D. Le Mignant, G. Chanan, P. Wizinowich, and M. van Dam, "Atmospheric Turbulence Characterization with the Keck Adaptive Optics Systems. I. Open-Loop Data," Appl. Opt. **42**, 3705-3720 (2003).

[8] Martin J. Booth, Mark A. A. Neil, and Tony Wilson, "New modal wave-front sensor: application to adaptive confocal fluorescence microscopy and two-photon excitation fluorescence microscopy," J. Opt. Soc. Am. A **19**, 2112-2120 (2002).

[9] T. Fusco, G. Rousset, J. Sauvage, C. Petit, J. Beuzit, K. Dohlen, D. Mouillet, J. Charton, M. Nicolle, M. Kasper, P. Baudoz, and P. Puget, "High-order adaptive optics requirements for direct detection of extrasolar planets: Application to the SPHERE instrument," Opt. Express 14, 7515-7534 (2006).

[10] David G. Kocher, "Twyman-Green Interferometer to Test Large Aperture Optical Systems," Appl. Opt. 11, 1872_1-1874 (1972).

[11] James Millerd, Neal Brock, John Hayes, Michael North-Morris, Matt Novak and James Wyant, "Pixelated Phase-Mask Dynamic Interferometer," Proceedings of SPIE **5531** (2004).

[12] James Wyant, "White Light Extended Source Shearing Interferometer," Appl. Opt. 13, 200-202 (1974).

[13] Robert M. Neal and James C. Wyant, "Polarization phase-shifting point-diffraction interferometer," Appl. Opt. 45, 3463-3476 (2006).

[14] Patrick Naulleau, Kenneth A. Goldberg, Sang H. Lee, David Attwood, and Jeffrey Bokora, "The EUV Phase-Shifting Point Diffraction Interferometer," CP521, Synchrotron Radiation Instrumentation: Eleventh US National Conference, edited by P. Pianetta, et al., American Institute of Physics 1-56396-941-6 (2000).

[15] John W. Hardy, Adaptive Optics for Astronomical Telescopes (Oxford, 1998).

[16] Raymond N. Wilson, Reflecting Telescope Optics Volume 2 (Springer, 1999).

[17] James Notaras, Carl Paterson, "Point-diffraction interferometer for atmospheric adaptive optics in strong scintillation," Optics Communications **281**, 360-367 (2008).

[18] James E. Millerd, Neal J. Brock, John B. Hayes and James C. Wyant, "Instantaneous phase-shift, point-diffraction interferometer," Proceedings of SPIE **5531** (2004).

[19] Daniel R. Neal, James Copland, David Neal, "Shack-Hartmann wavefront sensor precision and accuracy," Proceedings of SPIE Vol. 4779 (2002).

[20] F. Roddier, "Curvature sensing and compensation: a new concept in adaptive optics, " Appl. Opt. 27, 1223 – 1225 (1988).

[21] Marcos A. van Dam and Richard G. Lane, "Extended analysis of curvature sensing," J. Opt. Soc. Am. A 19, 1390-1397 (2002).

[22] Xi Fengjie, Jiang Zongfu, Xu Xiaojun, Hou Jing, and Liu Zejin, "Frequency analysis of wavefront curvature sensing: optimum propagation distance and multi-z wavefront curvature sensing,"

[23] James R. Fineup, "Phase retrieval algorithms: a comparison," Appl. Opt. 21, 2758 – 2769 (1982).

[24] Serge Meimon, Thierry Fusco, and Laurent M. Mugnier, "LIFT: a focal-plane wavefront sensor for real-time low-order sensing on faint sources," Optics Letters 35, 3036-3038 (2010).

[25] Brent L. Ellerbroek, "First-order performance evaluation of adaptive-optics systems for atmospheric-turbulence compensation in extended-field-of-view astronomical telescopes," J. Opt. Soc. Am. A 11, 783-805 (1994).

[26] Hart, M., Milton, N., Powell, K., Baranec, C., Stalcup, T., McCarthy, D. and Kulesa, C., "Wide-Field Image Compensation with Multiple Laser Guide Stars," Proceedings of the Advanced Maui Optical and Space Surveillance Technologies Conference, Editor. S. Ryan (2009).

[27] Hanshin Lee, "Optimal collimation of misaligned optical systems by concentering primary field aberrations," Optics Express 18, 19249 (2010).
[28] Hanshin Lee, "Modal analysis of focus-diverse point spread functions for modal wavefront sensing of uniformly illuminated circular-pupil systems," Optics Letters 36, 1503-1505 (2011).
[29] R. Noll, "Zernike polynomials and atmospheric turbulence," J. Opt. Soc. Am. 66, 207-211 (1976).
[30] Joseph W. Goodman, *Introduction to Fourier Optics* 3rd edition (Robert & Company, 2005).
[31] Simone Esposito, "Introduction to Multi-Conjugate Adaptive Optics systems, " C. R. Physique 6, 1039–1048 (2005).
[32] Benjamin Potsaid, Yves Bellouard, and John T. Wen, "Adaptive Scanning Optical Microscope (ASOM): A multidisciplinary optical microscope design for large field of view and high resolution imaging," Optics Express 13, 6504-6518 (2005).
[33] P. Kner, J.W. Sedat, D.A. Agard, and Z. Kam, "High-resolution wide-field microscopy with adaptive optics for spherical aberration correction and motionless focusing," *J Microsc*. 237(2), 136–147 (2010).
[34] Peter B. Stetson, "DAOPHOT - A computer program for crowded-field stellar photometry," Publications of Astronomical Society of the Pacific 99, p. 191-222 (1987).
[35] G.J. Hill, M.E. Cornell, D.L. DePoy, N. Drory, M.H. Fabricius, A. Kelz, H. Lee, J.L. Marshall, J.D. Murphy, T. Prochaska, S.E. Tuttle, B.L. Vattiat, R.D. Allen, G. Blanc, T.S. Chonis, K. Gebhardt, J.M. Good, D.M. Haynes, P.J. MacQueen, M.D. Rafal, M.M. Roth, R.D. Savage, J.M. Snigula," VIRUS: production of a massively replicated fiber integral field spectrograph for the upgraded Hobby-Eberly Telescope," Proc. SPIE, 8446-21 (2012).
[36] S.E. Tuttle, R.D. Allen, T.S. Chonis, M.E. Cornell, D.L. DePoy, G.J. Hill, H. Lee, J.L. Marshall, T. Prochaska, M.D. Rafal, R.D. Savage, B.L. Vattiat, "Initial results from VIRUS production spectrographs," Proc. SPIE, **8446**-221 (2012).
[37] H. Lee, et al., "VIRUS optical tolerance and production," Proc. SPIE, **7735**-140 (2010).
[38] H. Lee, G.J. Hill, S.E. Tuttle, B.L. Vattiat, "Fine optical alignment correction of astronomical spectrographs via in-situ full-field moment-based wavefront sensing," Proc. SPIE, **8450**-192 (2012).